applied sciences

MDPI

Article

Surface Strengthening of 30CrMoA Gear Journal Shafts by Roller Burnishing: Residual Stress Field Characterization, Parametric Analysis, and Multi-Objective Optimization

Yongmei Wang [1], Jiafu Ruan [2] and Xigui Wang [2,*]

[1] School of Motorcar Engineering, Heilongjiang Institute of Technology, No. 999, Hongqidajie Road, Daowai District, Harbin 150036, China; wyr20091207@163.com
[2] School of Mechatronics and Automation, Huaqiao University, No. 668 Jimei Avenue, Jimei District, Xiamen 361021, China; rjfnefu1993@126.com
* Correspondence: wyr20091207@126.com

Featured Application

A targeted roller burnishing technique is developed to harden the outer diameter of machined 30CrMoA gear journal shafts and eliminate detrimental surface tensile stresses. Through coupling finite element modeling, X-ray diffraction experiments, and responsesurface-based multi-objective optimization, a stable gradient compressive residual stress field is established, peaking at about 0.20 mm beneath the surface. The optimized rolling parameters markedly increase surface compressive stress and strengthened-layer thickness, with model predictions matching experimental measurements within 8.0% relative error, providing a reliable theoretical and technical basis for rolling-based surface strengthening of gear shafts.

Abstract

Residual tensile stresses are readily introduced into the surface layers of gear-shaft journals during machining, promoting fatigue crack initiation and propagation and degrading service reliability. This study investigates mechanical rolling strengthening of the outer cylindrical surfaces of 30CrMoA gear-shaft journals to improve residual stress distribution. Finite element (FE) simulations and X-ray diffraction (XRD) measurements were combined to characterize the rolling-induced residual stress fields and to elucidate the effects of rotational speed, indentation depth, and feed rate on the residual compressive stress magnitude and strengthened-layer thickness. Response surface models based on a central composite design (CCD) were established, and multi-objective optimization was performed to identify optimal rolling parameters. The results reveal a gradient residual compressive stress field in the surface layer, with the maximum compressive stress at approximately 0.20 mm below the surface, whereas slight residual tensile stresses develop in the deeper substrate to maintain self-equilibrium of the residual stress field. Indentation depth exerts the most pronounced influence, significant parameter interactions are observed, and the strengthening responses saturate over the investigated ranges. Experimental validation confirms that the optimized parameters simultaneously enhance the surface residual compressive stress magnitude and strengthened-layer thickness, with relative errors between predictions and measurements below 8.0%. The proposed model accurately describes the depth-dependent residual stress distribution, providing a theoretical basis and practical guidance for parameter design and optimization of mechanical rolling strengthening of 30CrMoA gear-shaft journals.

Keywords: surface mechanical deep rolling; residual stress; gear shaft journals; distribution characteristics; parameter optimization; finite element simulation

Check for updates

Academic Editor: Dario Croccolo

Received: 16 October 2026
Revised: 3 November 2026
Accepted: 5 November 2026
Published: 9 November 2026

Copyright: © 2026 by the authors. Licensee MDPI, Basel, Switzerland. This article is an open access article distributed under the terms and conditions of the Creative Commons Attribution (CC BY) license.

1. Introduction

Serving as critical elements in power transmission systems, gears are required to exhibit not only high manufacturing precision but also long-term service durability. During meshing, the shaft bearing surface undergoes severe alternating impact loading over extended operation, making it highly susceptible to bending and torsional deformation. Sustained cyclic bending stress progressively accumulates fatigue damage in the material, ultimately giving rise to crack initiation and substantially degrading the reliability and service life of gear drives [1–3]. Thanks to rapid advances in computing power, finite element analysis has matured into an indispensable aid for designing gear–shaft structures against fatigue. Nevertheless, exclusive dependence on structural optimization is constrained in two respects: the potential for further gains at the shaft journal remains intrinsically limited, and altering structural parameters propagates along the dimensional chains of adjacent mating components, producing knock-on effects that are difficult to accommodate within real-world manufacturing constraints [4]. Therefore, improving fatigue strength by refining the process route and optimizing its parameters currently offers a more practical and technically viable route [5,6].

To address demands in engineering fields, a variety of surface reinforcement approaches have been established up to now, while every method has its own suitable operating parameters and unavoidable restrictions [7,8]. Among these approaches, surface roller extrusion hardening stands out as a non-machining surface modification technique that delivers repetitive rolling forces to component surfaces through purpose-built rolling tools, typically made of quenched steel, hard alloy, or corundum, with shapes ranging from rollers and spheres to wheels (the related processing flow is shown in Figure 1) [9,10]. Apart from substantially lowering surface roughness, the process gives rise to a beneficial distribution of compressive residual stress field in the subsurface layer while simultaneously improving resistance to corrosion, wear, and fatigue, demonstrating strong potential for engineering practice [11].

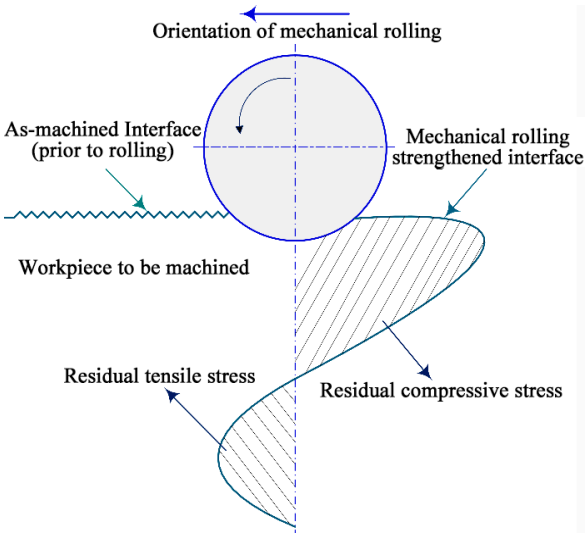


Figure 1. A visual representation outlining the operational steps of the rolling procedure.

Surface rolling hardening effectively improves the fatigue resistance of machine parts and has therefore gained wide acceptance in surface engineering. Researchers at Tianjin University's Internal Combustion Engine Research Institute, for example, applied localized rolling to strengthen the journals of gear shafts operating in 370Q and 376Q diesel engines [12,13]. Such treatment, when applied to the targeted shaft components, yields clear positive outcomes: the fatigue threshold of the journals that underwent rolling reinforce-

ment rises by 92.3 percent compared to those not subjected to this process, while the safety factor approaches a twofold increase [14]. Independently, Liuzhou Nanfang Automotive Cylinder Liner Factory carried out rolling strengthening trials on cylinder sleeves, while Henan Yingwei Dongfeng Machinery Manufacturing Co., Ltd. applied the same process to hub axle tubes; both trials confirmed significant improvements in product qualification rates and fatigue strength [15,16]. The strengthening treatment enables 300M steel to achieve a stress corrosion cracking (SCC) strength approaching the yield strength, together with a substantially elevated fracture threshold, which collectively contribute to its superior SCC resistance [17]. Post-repair rolling of heavy-duty components has also been explored at the Academy of Armored Force Engineering: after surfacing repair, the rolling process applied to the machined surface under optimized parameters produces a nanocrystalline layer, thereby increasing hardness, boosting wear resistance, and improving the residual stress profile [18,19].

To regulate the near-surface microstructure and stress state of LZ50 steel, rolling is carried out; the results showed that the process increases subsurface hardness while inducing pronounced compressive residual stresses [20]. The synergistic action of enhanced surface hardness and compressive residual stresses effectively delays the initiation of microcracks and impedes their propagation; by weakening the growth-promoting role of clustered microdefects, it thereby enhances the material's local resistance to fatigue [21]. The researchers observed that cracks consistently initiated from the specimen surface under high stress levels associated with relatively short fatigue lives, irrespective of surface processing [22]. Rolling, by contrast, imparted a favorable compressive residual stress field to the specimen surface, thus improving the material's fatigue performance.

For the low-strain, long-cycle performance range, crack initiation points in unprocessed samples are found just below the surface; in processed samples, however, these points moved to inner areas that lacked both residual compressive stress zones and hardened layers, which led to a notable enhancement in fatigue resistance [23]. Regarding rolled AA6110-T6 aluminum alloy, X-ray diffraction is used to characterize the residual stress profile as a function of depth, which is then correlated with the fatigue behavior of the steel. The alteration of residual stress when exposed to different temperatures and the related core principles are investigated [24,25]. Taken together, these findings demonstrate that rolling induces a deep compressive residual stress layer beneath the surface, which lowers the effective stress in service and suppresses fatigue crack initiation and early growth, thereby substantially improving the material's fatigue life [26,27]. Furthermore, applying rolling processing enhances the quality of the specimen's outer layer, decreases the unevenness of its exposed surface, creates smooth and continuous finished surface contours, effectively eases the build-up of localised internal tension, and cuts down the harmful impact brought by geometric indentations on fatigue resistance [28,29]. A stochastic rack-mounted vehicle-track dynamic framework that accounts for nonlinear wheel-rail and gear-rack contact interactions is developed to unpack the coupling mechanisms among terrain, wind, and vehicle systems under pulsating crosswinds. The findings indicate that gusty crosswinds negatively affect operational stability and gear–rack meshing, with these harmful impacts growing more severe as the slope becomes steeper; the safe wind velocity limits drop from 29 to 22.5 $m \cdot s^{-1}$ when the slope rises from 100‰ to 200‰ [30].

To sum up, the rolling reinforcement approach shows notable effects on refining surface microstructures, adjusting stress distribution patterns, and boosting surface quality, serving as a reliable method for enhancing fatigue resistance.

2. Materials and Experimental Procedures

2.1. Materials and Specimen Preparation

The shaft specimens are manufactured from 30CrMoA alloy steel, where E, $\sigma_{0.2}$, σ_b, ν, ρ, μ, and C denote the elastic modulus, yield strength, tensile strength, Poisson's ratio, density, friction coefficient, and specific heat capacity, respectively.

A scaled-down test piece, made of the same material and holding the same initial post-heat-treatment state, is used to carry out process-related experiments and measurements. Based on the principle of material similarity, a full-scale, high-precision gear shaft is selected as the reference prototype for specimen design, and the associated testing cost and duration are also considered. Table 1 summarizes the specific heat-treatment parameters adopted for the specimens that underwent rolling processing.

Table 1. Detailed specifications related to modulation technologies.

Item	Technical Indicators
Tensile strength (Longitudinal direction)	600 MPa
Surface roughness	Ra0.8
Surface hardness	HB220~260

2.2. Strengthening Mechanism of Surface Rolling

Mechanical rolling is fundamentally an elastoplastic contact process. When the contact stresses induced at the roller–specimen interface exceed the yield strength of the material, plastic deformation occurs in the surface layer of the specimen, resulting in the formation of a work-hardened layer and the development of a compressive residual stress field. According to Hertzian line-contact interface theory [31], the contact half-width, b, at the roller–specimen interface can be expressed as follows:

$$b = 2\sqrt{\frac{RP}{\pi L E^*}} \tag{1}$$

where P is the normal load applied during mechanical burnishing, R indicates the radius of the burnishing roller, L denotes the effective contact length of the burnishing roller, and E^* is the equivalent elastic modulus of the specimen material, which can be expressed as follows:

$$\frac{1}{E^*} = \frac{(1-v_1^2)}{E_1} + \frac{(1-v_2^2)}{E_2} \tag{2}$$

where E_1 and E_2 denote the elastic moduli of the mechanical rolling roller and the specimen material, respectively, and v_1 and v_2 are their corresponding Poisson's ratios.

The maximum contact pressure p_0 on the shaft surface during roller burnishing can be expressed as:

$$p_0 = \sqrt{\frac{PE^*}{\pi RL}} = \frac{2P}{\pi bL} \tag{3}$$

The distribution of force applied forms a half-oval shape and aligns at a right angle to the central line of the rolling component.

$$p(x) = p_0\sqrt{1-\left(\frac{x}{b}\right)^2} \tag{4}$$

This term stands for the horizontal distance measured from the center of the contact point.

When the pressure applied during rolling hits a specific threshold, the initial yield of a material takes place, as specified by the Tresca criterion, which is also known as the maximum shear stress theory:

$$P_Y = \frac{\pi RL(1.1\sigma_Y)^2}{E^*} \tag{5}$$

with σ_Y denoting the uniaxial yield strength of the material.

As long as the contact pressure remains below the yield strength, the contact is purely elastic and can be described by Hertz's theory, beyond this threshold, plastic deformation is initiated in the material.

The whole process of roll forming consists of three distinct phases: elastic deformation, elastoplastic deformation, and full plastic deformation. When rolling is performed on a specific journal, internal forces of a certain magnitude are generated within its structure. To counterbalance the thermal and centrifugal loading experienced in service, compressive residual stresses must be generated within the journal surface layer, a requirement that dictates applied stresses above the yield strength so as to induce plastic flow. Nonlinear material-related issues encompass scenarios that involve both elastic and plastic deformation behavior [32].

The deformation behavior of ductile materials can be described by the following mathematical expression:

$$\{d\varepsilon\} = \{d\varepsilon_p\} + \{d\varepsilon_e\} \tag{6}$$

where $d\varepsilon_e$ and $d\varepsilon_p$ are the plastic and elastic strain increments of the specimen material, respectively, with the elastic strain component governed by Hooke's law, expressed as:

$$\{d\varepsilon_e\} = [D_e]^{-1}\{d\sigma\} \tag{7}$$

where $[D_e]$ and $\{d\sigma\}$ are the elastic matrix of the specimen material and the residual stress increment, respectively, with the plastic component governed by the flow rule, given by:

$$\{d\varepsilon_P\} = d\lambda \frac{\partial F}{\partial \{\sigma\}} \tag{8}$$

Herein, this refers to the boundary that defines the range of stress states that a material can withstand before yielding, where the loading surface is represented here This framework employs the von Mises yield criterion. Subsequently, the increment-based connection between stress and strain for the ideal elastic-plastic model is presented in the subsequent formulation as shown below:

$$\{d\sigma\} = ([D]_e - [D]_P)\{d\varepsilon\} = [D]_{ep}\{d\varepsilon\} \tag{9}$$

Rolling only leads to localized microscopic plastic deformation, so it is hypothesized that this procedure will not change the overall elastic characteristics of the work piece. Whether a single roller or a roller array is adopted, the deformation is treated under plane-strain conditions. Given that the roller–specimen interaction is simplified to a line-contact configuration, the rolling pressure is treated as a concentrated line load, and the internal stress field induced within the specimen is described by the Flamant solution [33]:

$$\sigma_r = -\frac{2p_s \cos\theta}{\pi r},\ \sigma_\theta = 0 \tag{10}$$

$$\sigma_z = \nu(\sigma_r + \sigma_\theta) = -\frac{2\nu p_s \cos\theta}{\pi r} \tag{11}$$

$$\tau_{r\theta} = \tau_{\theta r} = 0,\ \tau_{rz} = \tau_{zr} = 0,\ \tau_{\theta z} = \tau_{z\theta} = 0 \tag{12}$$

where p_s is the line load intensity at the center of the contact, which relates to the rolling pressure p through:

$$p_s = \frac{p}{a} \tag{13}$$

where a denotes the contact distance corresponding to the rotation angle of the cylindrical burnishing roller.

Combining Equations (10)–(13) with the von Mises yield condition yields.

$$\sigma_s = \frac{\sqrt{2}}{2}\sqrt{(\sigma_\theta - \sigma_r)^2 + (\sigma_\theta - \sigma_z)^2 + (\sigma_r - \sigma_z)^2 + 6(\tau_{r\theta}^2 + \tau_{\theta z}^2 + \tau_{rz}^2)} \tag{14}$$

Then, the following is obtained:

$$r = \frac{2p_s\left(\sqrt{1-\nu+\nu^2}\right)\cos\theta}{\pi\sigma_s} \tag{15}$$

where σ_s denotes the von Mises yield strength of the test specimen and v is its Poisson's ratio. Therefore, microplastic deformation develops within a cylindrical zone beneath the line load during rolling. By equating the von Mises stress with θ, the depth of the microplastically deformed layer is linked to the rolling force as follows:

$$d = \frac{2p_s\sqrt{1-\nu+\nu^2}}{\pi\sigma_s} = \frac{2p\sqrt{1-\nu+\nu^2}}{\pi a\sigma_s} \tag{16}$$

When it comes to spherical rolling operations, the interaction between the spherical part and the processing material can be simplified to a point-shaped contact, and the rolling pressure is correspondingly treated as a force that is concentrated at a single point. The stress components within the specimen are derived through the application of the Boussinesq solution, as outlined in the subsequent expressions.

$$\sigma_\rho = \frac{p}{2\pi R^2}\left[-\frac{3\rho^3 x}{R^3} + \frac{(1-2\nu)R}{R+x}\right] \tag{17}$$

$$\sigma_\theta = \frac{(1-2\nu)p}{2\pi R^2}\left[\frac{x}{R} - \frac{R}{R+x}\right] \tag{18}$$

$$\sigma_x = \frac{3\rho x^3}{2\pi R^5} \tag{19}$$

$$\tau_{xr} = \tau_{rx} = -\frac{3p\rho x^2}{2\pi R^5} \tag{20}$$

$$\tau_{r\theta} = \tau_{\theta r} = 0; \quad \tau_{\theta x} = \tau_{x\theta} = 0 \tag{21}$$

$$R^2 = x^2 + \rho^2 = x^2 + y^2 + z^2 \tag{22}$$

Applying the von Mises yield criterion to Equations (17)–(22), with $y = 0$ and $z = 0$ imposed at the centerline, yields an explicit relationship between the depth of microplastic deformation and the applied rolling force:

$$d = \sqrt{\frac{p(2\nu+5)}{4\pi\sigma_s}} \tag{23}$$

In fracture-mechanics terms, surface cracks and crack-like defects propagate under cyclic loading only when the crack-tip stress intensity factor range exceeds the material's fatigue crack-growth threshold. When mean-stress effects are considered, the corresponding threshold range is given by [34,35]:

$$\Delta K_{th} = \frac{1.2(\Delta K)}{1 + 0.2(1+R)/(1-R)} \tag{24}$$

Herein, this value refers to the mean level of force exerted repeatedly under fluctuating loading conditions.

Residual compressive stresses counteract the mean stress from external cyclic loads, thereby reducing the effective crack-tip stress intensity factor range and raising the threshold for fatigue crack growth, crack propagation therefore demands a higher applied stress under identical loading conditions. This mechanism accounts for the improved fatigue resistance of components containing cracks.

2.3. Mechanical Roll Forming Experiment

A CAK3665 CNC lathe (Shenyang Machine Tool Co., Ltd., Shenyang, China) was used as the experimental platform for the mechanical rolling tests, as shown in Figure 2. The lathe provides a steplessly variable spindle speed of 20–3000 r/min through variable-frequency control. The X-axis provides a travel of 230 mm, a traverse speed of 4.0 m/min, and a positioning repeatability of 0.012 mm; the corresponding values for the Z-axis are 660 mm, 8.0 m/min, and 0.016 mm, respectively. These specifications satisfy the control-accuracy requirements for the indentation depth, specimen rotational speed, and feed rate in this study. During the experiments, the rolling tool was secured to the X-axis tool carriage (slide) using a fixture, and a circular roller was brought into contact with the journal surface of the gear shaft at a prescribed indentation depth. The specimen was rotated at a constant speed by the machine spindle, while the rolling tool was fed axially along the journal at a prescribed feed rate, thereby producing a continuous helical rolling track on the journal surface. Under a constant externally applied load, normal contact pressure was generated at the roller–journal interface. When the resulting contact stress exceeded the yield strength of the specimen material, directional plastic flow occurred in the surface layer of the journal. The indentation depth was adjusted in real time by the CNC system and directly governed the contact stress and the degree of plastic deformation within the rolled region.

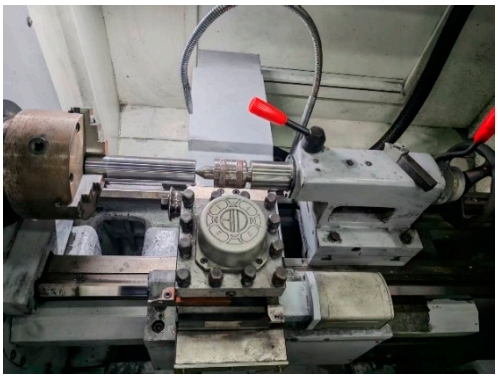


Figure 2. Rolling test platform.

To minimize the influence of local surface heterogeneity on the measurement results, three measurement cross-sections were defined at axial positions near both ends and at the mid-length of the effectively rolled section of the gear shaft. Three measurement regions were selected at 120° intervals along the circumference of each cross-section, yielding a total of nine measurement regions, each covering an area of 3×3 mm^2. All measurement regions were located on the effectively rolled surface, while clamping transition zones, unmachined edges, and areas with evident macroscopic defects were avoided. Measurements were performed in triplicate in each region under identical testing conditions, and the arithmetic mean of the three measurements was taken as the regional result. The final results are reported as the mean ± standard deviation of the nine regional results.

The residual stress state in the surface layer was characterized by X-ray diffraction (XRD) using a PROTO LXRD stress analyzer (Proto Manufacturing Ltd., LaSalle, ON, Canada). The internal stress distribution across the layer's depth was then characterised by sequentially removing tiny surface layers using a PROTO 8818-V3 electropolishing device (Proto Manufacturing Ltd., LaSalle, ON, Canada) and measuring stress levels after every removal, generating a full profile of stress variation through the depth direction. Deep-focus microscopy was employed to examine the surface microstructure both prior to and subsequent to rolling; the acquired imagery delivered the deformed layer's thickness and grain shape for every parameter combination and served to investigate rolling-triggered

plastic deformation and grain refinement. Table 2 details the experimental design used to investigate the effects of penetration depth, feed rate, and specimen rotational speed on the surface residual stress and the depth of the stress-affected layer.

Table 2. Plan and findings from the experiment.

No.	Rolling Process Parameters			Associated Parameters	
	Rolling Indentation Depth (mm)	Rolling Feed Rate (mm/r)	Specimen Rotational Speed (r/min)	Residual Stress in the Surface Layer of the Shaft Journal (MPa)	Depth of the Contact-Stress-Affected Surface Layer (mm)
1	0.05	0.05	600	−405.97	0.573
2	0.07	0.05	600	−497.61	0.591
3	0.10	0.05	600	−567.94	0.795
4	0.15	0.05	600	−538.52	0.807
5	0.20	0.05	600	−490.36	0.818
6	0.10	0.01	600	−498.73	0.628
7	0.10	0.03	600	−533.67	0.688
8	0.10	0.06	600	−588.32	0.741
9	0.10	0.08	600	−515.61	0.658
10	0.10	0.05	120	−535.63	0.624
11	0.10	0.05	360	−553.47	0.677
12	0.10	0.05	720	−584.75	0.714
13	0.10	0.05	840	−582.72	0.813

Stress evaluation followed the $\sin^2\psi$ approach with Cr–Kα radiation (λ = 2.2910 Å, 30 kV, 25 mA). The peak from the ferrite crystal's (211) planes (at a two-theta value roughly 156 degrees) was measured across eleven different tilt angles, ranging from minus 45 to plus 45 degrees, using a 1.0-mm circular collimator set at the center of the rolled strip; the axial and circumferential directional components were collected in distinct measurement runs. After background removal and Lorentz–polarization–absorption (LPA) correction, peak locations were extracted by cross-correlation, and stresses were computed with the ferritic-steel X-ray elastic constants ($½S_2 = 5.81 \times 10^{-6}$ MPa^{-1}, $S_1 = -1.27 \times 10^{-6}$ MPa^{-1}); a stress-free annealed iron powder served as the calibration reference. For measuring data at varying depths, superficial layers were removed via electrolytic polishing in a saturated sodium chloride solution at room temperature and 20 volts, this method prevents mechanical stress introduction. A roughly 3 × 3 mm^2 area around the measurement point was shielded, and each material removal step (20 to 50 micrometres) was verified using a micrometer with a ±2 micrometer margin of error. Depth-specific measurement points were set at 0, 0.02, 0.05, 0.10, 0.20, 0.30, 0.50, 0.80 and 1.00 mm; given the small area subjected to electropolishing, no adjustments for stress redistribution needed to be performed. For each specimen, three measuring points evenly distributed along the perimeter were selected, with their respective values averaged together (the spread of these values fell within ±25 MPa); meanwhile, the total uncertainty stemming from measurement consistency, calculated through repeated checks on a stress-free reference sample, stood at ±20 MPa. The as-rolled surfaces (Ra = 0.4–0.8 μm) were tested without mechanical polishing, only a simple degreasing step with acetone was applied prior to testing, so as to preserve the original residual stress state.

Rolling involves several nonlinear effects, material and geometric nonlinearities, contact behavior, friction, and thermal coupling, making full-process simulation computationally demanding. The operating conditions must therefore be appropriately simplified to lower the computational cost while preserving accuracy and ensuring convergence [36,37]. For this purpose, a segmented modeling strategy is used, with the roller assumed to be rigid owing to its substantially higher stiffness than the specimen [38,39]. Throughout the entire forming operation, the roller stays in the elastic deformation range, while the specimen experiences substantial plastic deformation. Under the highest contact pressure analyzed

in this investigation, the local elastic flattening (of the Hertzian type) of the roll's surface measures just a few micrometres, this value is extremely small (far less than 0.1%) when compared to the millimetre-scale plastic shape changes and thickness reduction in the specimen material. As a result, the roll's surface form, the size and configuration of the contact area, and the related distributions of contact force and frictional resistance are barely impacted by the roll's elastic changes. In the finite-element modeling of rolling, roll bending, ring rolling, and cold roll forming processes that involve coupled material, geometric, contact nonlinearities as well as friction and heat transfer, it has become a standard approach to treat the roll as a rigid body, either from an analytical standpoint or using discrete methods. Modeling the roll as a rigid structure removes unnecessary elastic motion variables, lowers the computing burden related to contact searching and equation calculations, and enhances the stability of both explicit and implicit nonlinear solvers; at the same time, the contact rules, frictional stresses, and heat exchange at the interface between the roll and specimen are still fully applied through the rigid reference surface. The process of enhanced material modification studied here features contact zones and applied loads that are within a suitable range, with the key metrics of focus being the specimen's deformation characteristics, thermal states, and interactions at the contact boundary. Based on the characteristics observed in this particular work's strengthening procedure, using a rigid rolling model is thus logical and well-suited for the current research work.

The three-dimensional model is illustrated in Figures 3 and 4. It shows the overall structure of the main components involved in the simulation setup, which lays the foundation for the following parameter settings of each part. A three-dimensional model of the 30CrMoA specimen is built with overall geometry of 40 mm (length) × 16 mm (width) × 20 mm (height). To reproduce the experimental setup, the rolling roller diameter, fillet radius, and center height are set to 65 mm, 2.0 mm, and 30 mm, respectively. The rolling process is simulated by fixing all degrees of freedom on the bottom face of the specimen, thereby eliminating rigid-body motion, while the roller is driven in simultaneous rotation and reciprocating translation along the surface. After each reciprocating stroke, the roller shifted laterally by a fixed increment to progressively cover the whole processing area. C3D8R elements (eight-node linear bricks with reduced integration) are adopted for the specimen, together with enhanced hourglass control, thereby avoiding shear and volumetric locking while ensuring stable contact and higher computational efficiency.

A mesh convergence analysis is conducted to confirm that the finite element outcomes are not dependent on the specific mesh used. Three distinct element sizing schemes are explored: a relatively coarse setup with edge lengths around 2.0 mm applied to the contact area (totalling 5348 individual elements), a moderate scheme with an approximate edge length of 1.0 mm (totalling 24,975 elements), and a refined scheme with an edge length roughly 0.5 mm (totalling 67,126 elements). A targeted refinement approach for the grid setup is utilized, where the smallest grid units are placed in the area where the roller makes contact and shifts, while larger grid units are applied to areas not within the range of deformation, this setup achieves a good balance between calculation accuracy and speed. Eight-node thermally coupled brick elements (C3D8RT), which incorporate reduced integration and hourglass control, are adopted for all computations, a choice dictated by their ability to accommodate the material, geometric, and contact nonlinearities involved in rolling. The mesh convergence results are summarized in Table 3. Compared with the fine grid, the values of the assessed parameters for the intermediate grid differ by less than 1% each, while those for the rough grid relative to the intermediate grid show gaps of 16.33% and 9.89% separately. Thus, this study selects the medium-sized grid for all rolling numerical simulations presented in this work. To address potential element issues

in large-deformation rolling scenarios, we implement an arbitrary Lagrangian-Eulerian (ALE) adaptive meshing approach, which avoids severe element distortion and enhances the confidence in the numerical simulation outcomes.

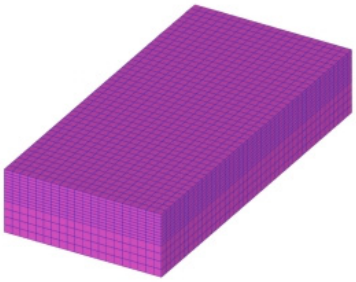


Figure 3. Three-dimensional model of the specimen.

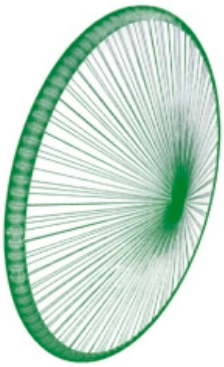


Figure 4. Three-dimensional model of the roller.

Table 3. Results of the mesh convergence analysis.

Parameters	Grid Level	Number of Units	Residual Stresses on the Contact Surface (MPa)	Magnitude of Change (%)	Stress Depth (mm)	Magnitude of Change (%)
Rolling depth (0.10 mm);	Coarse mesh	5348	−489.275	-	0.79816	-
Feed rate (0.05 mm/r);	Medium mesh	24,975	−569.16	16.33%	0.71923	9.89%
Specimen speed (600 r/min)	Fine mesh	67,126	−573.842	0.82%	0.71457	0.65%

When conducting analyses focused on residual stress, the finite element grid is also adjusted locally, with finer divisions applied where deformation effects are more pronounced. Within the machined surface area, where intensive plastic deformation and sharp residual-stress gradients develop, smaller mesh elements (specifically sized at 0.50 mm) are deployed; for the untouched base material zone, which is distant from the stress-affected area and only displays slight stress gradients, larger mesh elements (2.0 mm in size) are utilized, with seamless size changes between the two zones to maintain good mesh performance. Mesh convergence is examined at five element sizes (0.10–1.00 mm), with the peak residual compressive stress and strengthened layer thickness as evaluation metrics. Variations in both metrics remained below 2.0% as the element size decreased from 0.50 to 0.10 mm, demonstrating that the solution is essentially mesh-independent at 0.50 mm; finer meshes would inflate the element count and computational expense substantially. By contrast, coarser meshes (>0.50 mm) yielded marked deviations in residual stress and are therefore non-convergent. Accordingly, 0.50 mm elements are applied to the processed surface layer throughout the following numerical experiments.

Since the rollers are simulated as rigid entities, they do not necessitate the creation of a mesh or the specification of material attributes. Hexahedral elements are used for the specimen. A graded mesh layout, combining local refinement with size-controlled transition, is employed to balance accuracy and computational cost: fine elements are placed on the processed surface, and coarser ones on the unprocessed bottom region. The translational movement and forward progress of the roller are set via specified movement trajectories, while every other independent motion component is restricted. Functions that change over time are set to define the movement-related parameters, which in turn set up the boundary conditions for the roller.

Choosing a suitable time step holds great significance: a step that is too large might lead to noticeable mesh deformation and problems with convergence, while a step that is too small will dramatically extend the total computing time. To adequately resolve the steep gradients in the contact zone, the time step is restricted such that the roller advanced by less than 1/10 of a characteristic element length per increment, an increment size of 1×10^{-4} s is adopted, and the total increment count followed from the simulated process duration. Output file size is limited by writing results at every 50th increment, while preserving all data needed for post-processing [40]. The Johnson–Cook constitutive model captures the deformation response of the shaft-journal surface layer by incorporating strain hardening, strain-rate sensitivity, and thermal softening across a broad range of strain rates. In this study, the model is adopted to describe the reduction in flow stress in the surface layer induced by adiabatic temperature rise during the plastic deformation of 30CrMoA test specimens [41,42]. Taking the Johnson–Cook constitutive equation into account, the flow stress in the surface layer is expressed as:

$$\sigma = [A + B\varepsilon^n][1 + C\ln\varepsilon^*][1 - (T^*)^m] \tag{25}$$

where A the yield stress of the test specimen, B, n, C, m, and ε denote the strain-hardening coefficient, strain-hardening exponent, strain-rate sensitivity coefficient, thermal softening exponent, and equivalent plastic strain of the strengthened layer, respectively, B is the strain hardening coefficient, n is the strain hardening exponent, C is the strain-rate sensitivity coefficient, m is the thermal softening exponent, ε is the equivalent plastic strain, ε^* is the normalized equivalent plastic strain rate, and T^* is the dimensionless temperature. The normalized strain rate and the dimensionless temperature are defined as follows:

$$T^* = \frac{T_{\text{room}} - T}{T_{\text{room}} - T_{\text{melt}}} \tag{26}$$

where T, T_{room}, and T_{melt} denote the current, room, and melting temperatures, respectively.

At ambient temperature, the thermal softening term in the Johnson–Cook model equals unity, so that the model reduces to the simplified form presented below [43]. Table 4 lists the constitutive parameters used in the simulations.

$$\sigma = (A + B\varepsilon^n)(1 + C\ln\varepsilon^*) \tag{27}$$

Table 4. Johnson–Cook constitutive parameters of the 30CrMoA steel shaft journal.

A (MPa)	B (MPa)	C	m	n	ε^*/s^{-1}
800	550	0.02	1.20	0.20	1.0

Samples used in the study are fabricated using 30CrMoA steel, which underwent identical thermal processing as the components subjected to simulation analysis. This procedure yields a tempered sorbite-based microstructure, and the hardness values and tensile strength of this steel align with the specifications set for quenched and tempered

30CrMoA steel. Since rolling is performed at room temperature, the predicted temperature rise is marginal (a very low homologous temperature), the thermal-softening term in the Johnson–Cook model reduces to unity and can be omitted, yielding the following simplified expression for the flow stress [44], with the constitutive parameters listed in first table of Section 3.3. The nonlinear system is resolved using a sparse direct solver in conjunction with Newton–Raphson iteration.

3. Results and Discussion

3.1. Through-Depth Distribution Characteristics of Residual Stresses

Along the depth direction, the residual stress profile exhibits a well-defined four-zone structure: a surface layer of moderate compressive stress, a subsurface zone where the stress reaches its peak, a transition region of gradual decay, and an almost stress-free core [45]. Such a distribution pattern can be attributed to the residual stress generation mechanism associated with elastoplastic contact deformation. Figure 5 illustrates that the reinforcement brought about by mechanical rolling only affects the area of the specimen close to its surface. When subjected to concentrated contact pressure, the peak of von Mises stress appears below the surface, matching the characteristics of a standard Hertzian stress distribution; consequently, plastic deformation starts in the layer just under the surface, and the highest value of plastic strain is also located beneath the surface.

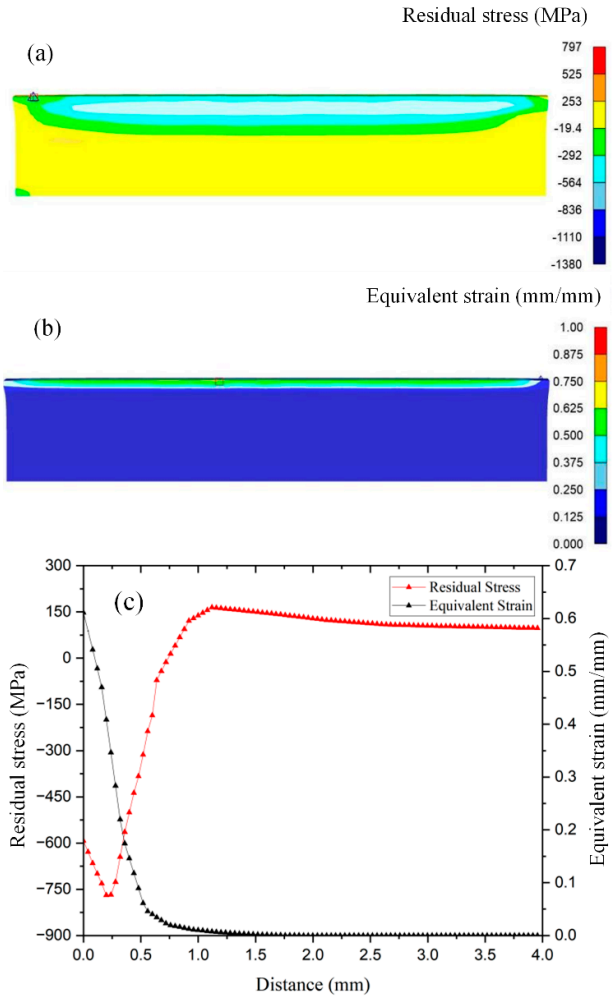


Figure 5. Residual stress and equivalent plastic strain in the cross-section under the standard process parameters. (**a**) Residual stress in the surface layer; (**b**) Strengthening-induced equivalent plastic strain; (**c**) Variation curve.

After unloading, elastic recovery of the plastically deformed region is impeded by the adjacent material, and the resulting incompatibility gives rise to a self-equilibrating residual stress field, the essence of the eigenstrain mechanism. A larger plastic strain with a steeper gradient enhances the elastic constraint exerted by the surrounding elastic material, thereby elevating the compressive residual stress. The compressive surface stress dips a little below the subsurface peak because (i) the traction-free state of the free surface partially relieves the near-surface plastic strain, lessening the constraint, and (ii) work hardening enhances the flow strength of the near-surface material. Within the plastic zone's outer region, the material undergoes only elastic deformation and fully returns to its original state when unloaded, leading to a sharp drop in compressive residual stress as it approaches the plastic zone's boundary where it reaches the base material's stress level. The inflection point of the measured residual stress profile is in close agreement with the plastic zone boundary forecast by the finite element model, thereby validating the simulation results.

This lower surface stress arises because the unconstrained free surface experiences substantial plastic flow during rolling, enabling partial relaxation via dislocation slip and grain rotation. At the subsurface location of maximum plastic deformation, where constraint from the surrounding elastic zone is strongest, the peak compressive residual stress develops; during unloading, the plastically deformed layer hinders the elastic recovery of the adjacent material, thereby giving rise to this peak. This subsurface zone serves as the main strengthening layer, suppressing stable crack growth and lowering the SIF at the crack tip. At greater depths, the residual stress vanishes, leaving the core material essentially unaffected. Self-equilibrium is maintained across the stress profile: small tensile stresses in the underlying material balance the surface compression; given that the strengthened layer occupies only a small fraction of the specimen thickness, their magnitude is negligible and the bulk mechanical properties remain intact.

Taken together, these findings reveal that rolling introduces a deep-reaching compressive residual stress field below the journal surface, whose peak occurs within the subsurface layer. This zone coincides with the region of stable fatigue crack growth, where cracks initiate and propagate under cyclic loading. The compressive residual stress field thus generated is anticipated to enhance the fatigue performance of the specimen; however, direct fatigue experiments are beyond the scope of this investigation. The even stress distribution along the axis maintains consistent strengthening performance throughout the whole length of the shaft, laying a stress-related groundwork for the prolonged working stability of the gear. This kind of common distribution also acts as a basis for future research on how process factors affect results, and for building parametric models.

3.2. Single-Factor Analysis of Process Parameters Affecting Residual Stress

To further clarify the separate effects of each strengthening process parameter, controlled-variable tests were conducted on the strengthening process, with all other associated factors maintained at their mid-range levels. By systematically varying the penetration depth, feed rate, and rotational speed of the specimen, the variations in the surface compressive residual stress of the shaft journal and the strengthened-layer depth with respect to these parameters were analyzed, from which the effective operating range of each process parameter and the corresponding plastic saturation behavior were determined.

3.2.1. Near-Surface Residual Stress Fields at Different Indentation Depths

To elucidate the dependence of the residual stress field on indentation depth, indentation experiments were conducted at five depths (0.05, 0.07, 0.10, 0.15, and 0.20 mm), while the specimen rotational speed and feed rate were maintained constant at 600 r/min and 0.05 mm/r, respectively.

The through-depth distributions of residual stress for these five cases are plotted in Figure 6. Figures 7 and 8 plot the surface residual stress and the strengthened-layer depth, respectively, as functions of the penetration depth. As shown in Figure 6, the five distributions follow a similar trend: a moderate compressive stress at the surface, rising steadily with depth to a subsurface peak at 0.2–0.4 mm, then decays gradually to zero near 0.8 mm and turns tensile (100–180 MPa) at depths beyond approximately 1.5 mm, offsetting the compressive field induced by surface plastic deformation. As penetration depth increases, the full profile is displaced in the negative direction, characterized by a higher subsurface compressive peak and a deeper compressive (plastically deformed) layer.

As illustrated in Figure 7, the residual compressive stress developed on the journal surface remains as low as −430.96 MPa when the penetration depth is only 0.05 mm. This phenomenon can be rationalized as follows. At such a shallow indentation, the near-surface material undergoes only limited plastic deformation, so that both dislocation multiplication and grain refinement are suppressed; meanwhile, during unloading of the rolling tool and the subsequent elastic recovery of the surface, the weak elastic constraint is insufficient to sustain a high compressive residual stress. As the penetration depth increases from 0.05 mm to 0.10 mm, the surface compressive residual stress rises monotonically, reaching −592.93 MPa. The deeper indentation enlarges both the contact force exerted by the roller and the burnished area on the test specimen, thereby triggering extensive irreversible plastic flow in the subsurface material; the resulting lattice distortion is tightly confined by the adjacent elastic matrix, which is macroscopically reflected in the progressive build-up of compressive residual stress.

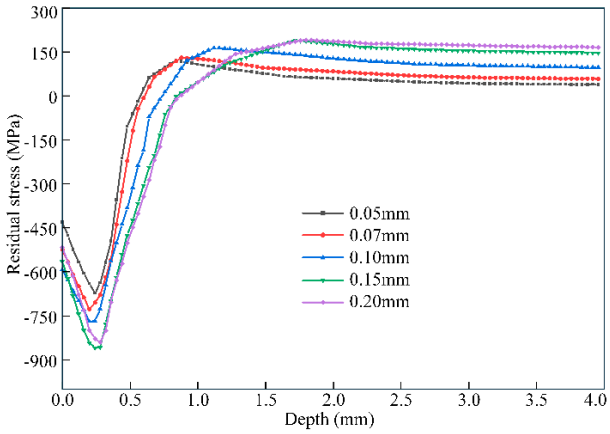


Figure 6. Depth profiles of residual stress for different penetration depths.

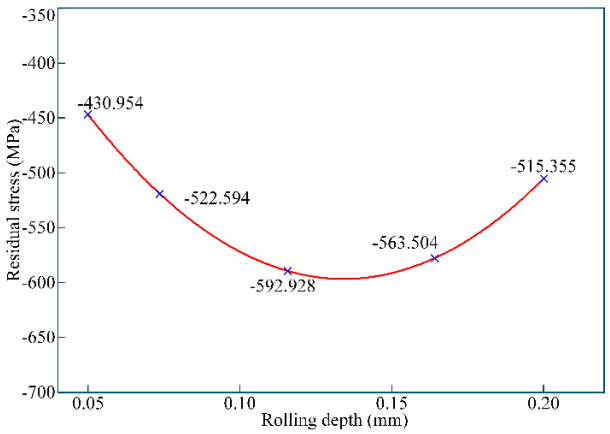


Figure 7. Surface residual stress versus penetration depth.

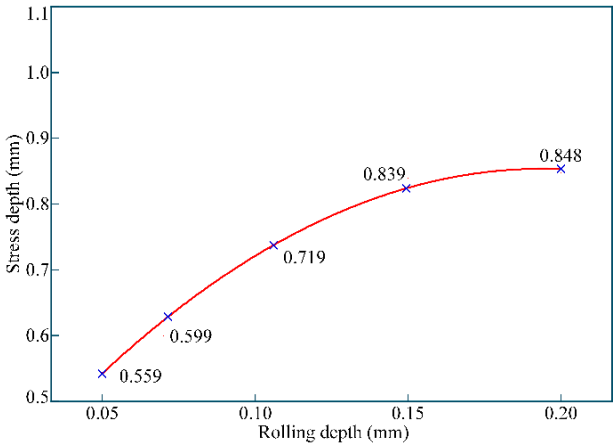


Figure 8. Strengthened layer depth versus penetration depth.

Nevertheless, once the penetration depth exceeds 0.10 mm, the surface compressive residual stress exhibits a slight downward trend, decreasing to −563.60 MPa at 0.15 mm and further to −515.36 MPa at 0.20 mm. Under excessive penetration, the surface metal experiences severe plastic deformation, which causes local microstructural damage such as microcracks and material pile-up. The resulting stress relaxation partially counteracts the accumulation of compressive residual stress. The increased plastic strain gradient across the strengthened layer slightly redistributes the self-equilibrating stress between the work-hardened layer and the substrate, thereby lowering the final compressive residual stress. As shown in Figure 8, the strengthened layer depth rises rapidly in the initial stage and then levels off, approaching saturation, with increasing penetration depth. The indentation depth remains as shallow as 0.559 mm at a penetration of 0.05 mm, rises in an approximately linear manner to 0.839 mm at 0.15 mm, and then levels off: at a penetration of 0.20 mm, the depth reaches only 0.848 mm, an increase of less than 0.02 mm, signifying that the plastic deformation has become saturated. Such saturation can be attributed to the pronounced constraint exerted by the journal substrate, which prevents the rolling load from being efficiently transferred into the underlying material.

3.2.2. Trends in Surface Residual Stress with Varying Specimen Rotational Speed

In this study, the effect of specimen rotational speed on the surface residual stress was examined through single-factor experiments, with the penetration depth and feed rate maintained at 0.10 mm and 0.05 mm/r, respectively. The rotational speed was set to five levels: 120, 360, 600, 720, and 840 rpm. Consequently, a further increase in penetration produces virtually no additional expansion of the compressive stress-affected zone.

The resulting through-depth residual stress profiles, surface residual stresses, and strengthened layer depths are shown in Figures 9–11. Figure 9 reveals that all five distributions exhibit a similar pattern, with the peak compressive stress consistently located in the subsurface layer; as the speed increases, nevertheless, the whole profile shifts downward and the peak compressive stress grows. When the roller operates at slower turning speeds, it stays at each spot around its circumference for a longer time, leading to a sharper local spatial change in plastic deformation. This sharp gradient, in turn, facilitates cyclic plasticity and elastic shakedown of the surface layer when subjected to repeated rolling passes, consequently easing some of the residual compressive stress generated.

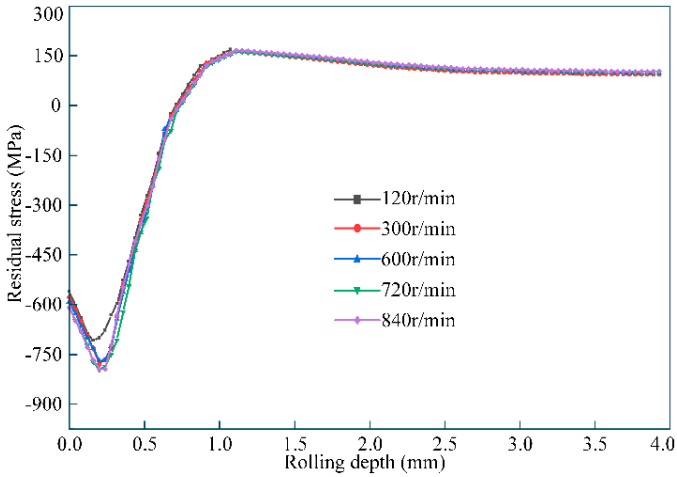


Figure 9. Residual stress versus depth at different specimen rotational speeds.

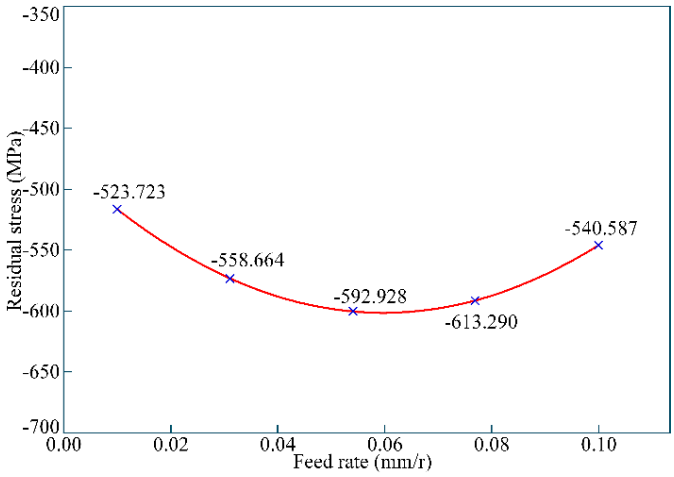


Figure 10. Surface residual stress versus specimen rotational speed.

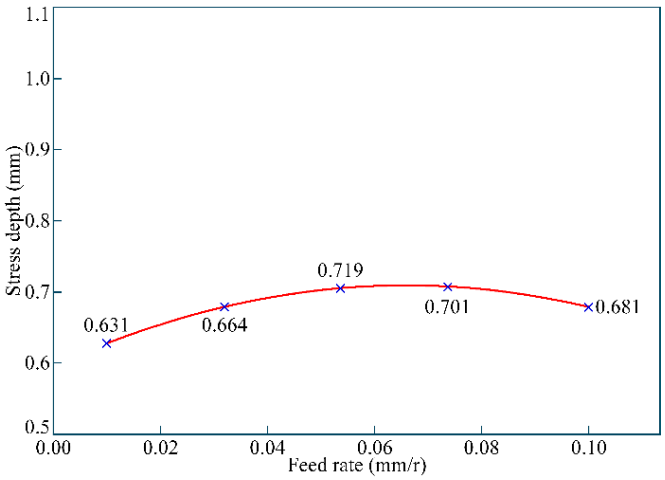


Figure 11. Strengthened layer depth versus specimen rotational speed.

As presented in Figure 10, the surface compressive residual stress equals −560.62 MPa when the test specimen rotates at 120 r/min. Raising the rotational speed to 360 r/min produces a slight increase in this stress, to −578.46 MPa. As the speed continues to climb, the compressive stress peaks at −609.73 MPa at 720 r/min; once the rotational speed exceeds this level and reaches 840 r/min, however, the stress undergoes a slight decline to

−607.70 MPa. Below the optimum speed, the compressive residual stress from subsurface plastic deformation partially relaxes, reducing the effective strengthened layer depth; a moderate speed increase, by contrast, mitigates localized frictional heating, transmits the rolling load deeper into the subsurface layer, and expands the plastically deformed zone, whereas at excessively high speeds the contact duration is too short for plastic deformation to fully develop in a single pass, resulting in a slight decrease in the strengthened layer depth.

With increasing rotational speed, the contact time shortens and the plastic strain gradient decreases, allowing the compressive residual stress from plastic deformation to be retained more fully [46,47]. Accordingly, the surface stress remains insensitive to speed in the low-speed range (varying by less than 20 MPa) but rises moderately at medium-to-high speeds, where higher speeds suppress cyclic plastic accumulation during repeated rolling. Beyond 720 r/min, excessive roller–specimen sliding promotes local micro-slip and slight frictional damage, causing the compressive residual stress to drop marginally. Figure 11 further demonstrates that the strengthened layer depth exhibits a clear speed-dependent trend: it starts at 0.674 mm at 120 r/min, climbs continuously to a peak value of 0.745 mm at 720 r/min, and then declines marginally to 0.734 mm when the speed reaches 840 r/min. Relative to the penetration depth, the rotational speed of the test specimen exerts a less pronounced influence on the residual stress field, since it governs the plastic deformation only in an indirect manner—namely, through the rolling contact duration and the temperature rise generated during the strengthening process. Balancing the strengthening effectiveness against the stability of the rolling process, the rotational speed is accordingly determined to lie within the optimal range of 600–720 r/min, in which a high surface compressive residual stress can be attained together with a sufficiently deep strengthened layer.

3.2.3. Residual Stress Response of the Surface Layer to Variations in Rolling Feed Rate

For the single-factor experiments, five feed rate levels are considered: 0.01, 0.03, 0.05, 0.07, and 0.10 mm/r, while the penetration depth and specimen rotational speed are held constant at 0.10 mm and 360 rpm, respectively. Figure 12 presents the through-depth residual stress profiles, the surface residual stress is illustrated in Figure 13, while the depth of the strengthened layer is presented in Figure 14. Figure 12 illustrates that the axial overlap ratio between adjacent rolling passes, and hence the magnitude of plastic strain accumulated in the near-surface layer, is governed by the feed rate. Raising the feed per revolution increases the pitch between successive tracks, so each surface location is rolled fewer times, and the accumulated plastic strain remains limited.

Conversely, lowering the feed narrows the track spacing and enlarges the overlap, so individual surface points undergo multiple rolling passes; plastic strain therefore builds up progressively, shifting the surface stress state toward higher compressive (i.e., more negative) values. However, an excessively small feed causes the tool to traverse the same region repeatedly: heat generated by the process then accumulates faster than it dissipates, markedly raising the surface-layer temperature, and the cyclic plastic deformation from repeated passes partially relaxes the compressive residual stress formed earlier; consequently, the surface compressive stress decreases.

At intermediate feeds of 0.05–0.07 mm/r, moderate pass overlap and limited temperature rise allow plastic strain accumulation to reach its optimum, so the surface compressive residual stress peaks. Figure 13 illustrates the non-monotonic dependence of the journal surface residual stress on feed rate. The residual stress is −523.72 MPa at 0.01 mm/r and becomes progressively more compressive as the feed rate increases, reaching −613.29 MPa at 0.07 mm/r. Beyond this feed rate, however, the magnitude of the residual compressive stress decreases markedly, with a value of −540.59 MPa recorded at 0.10 mm/r. This reduction can be attributed to the gaps that develop between successive axial rolling tracks at feed rates

above 0.07 mm/r. Consequently, some regions of the journal surface undergo only a single rolling pass or receive insufficient compaction, resulting in inadequate plastic deformation and weaker residual compressive stress.

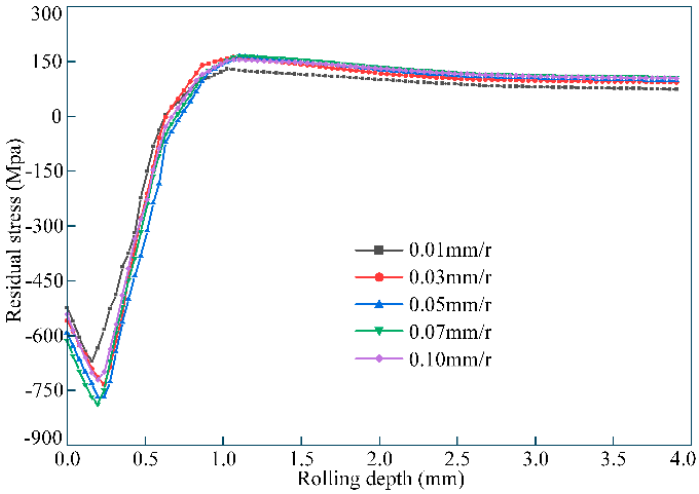


Figure 12. Through-depth residual stress distributions at different feed rates.

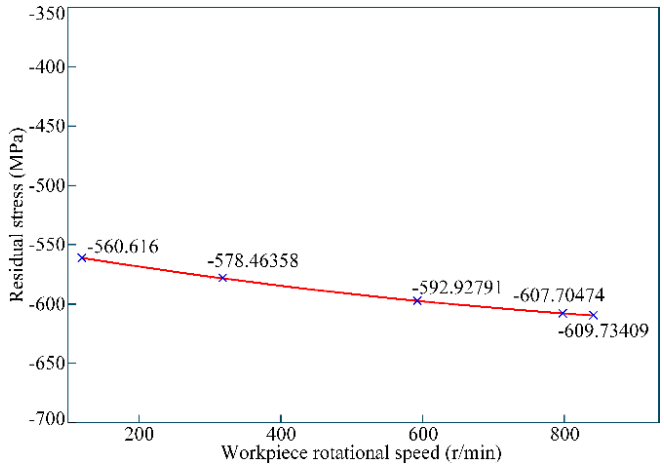


Figure 13. The influence of feed speed on remaining surface tension fields.

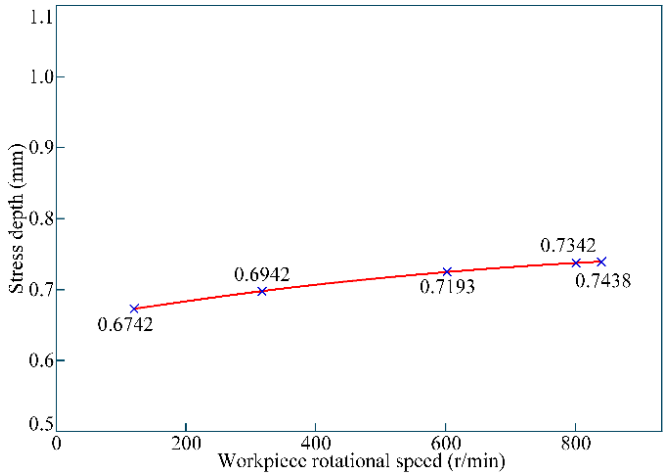


Figure 14. Effect of feed rate on strengthened layer depth.

Figure 14 further illustrates the effect of feed rate on the depth of the strengthened layer. At excessively low feed rates, repeated rolling over the same region causes substantial

surface heating. The resulting thermal relaxation of compressive stresses in the subsurface region consequently reduces the thickness of the strengthened layer. Within the moderate feed-rate range, plastic strain builds up evenly and the rolling force penetrates sufficiently far into the material, so the compressive-stress layer reaches its greatest depth.

At the high end of the feed-rate range, successive axial paths no longer overlap completely, and plastic strain remains restricted to an extremely shallow surface zone, so the compressive-stress layer becomes much thinner. The quantitative data confirm this trend: the strengthened layer depth reaches only 0.631 mm at 0.01 mm/r, attains its maximum of 0.719 mm at 0.05 mm/r, and decreases to 0.680 mm at 0.10 mm/r. A comprehensive consideration of the surface residual stress and the strengthened layer depth therefore suggests maintaining the feed rate within 0.05–0.07 mm/r: an overly small feed prolongs the process and aggravates the cyclic plasticity induced by repeated rolling, while an overly large feed results in non-uniform axial hardening and a pronounced reduction in the overall compressive residual stress.

3.2.4. Comparative Analysis of the Surface Rolling Strengthening Process Parameters

Based on the maximum changes in surface residual stress and strengthened-layer depth observed in the single-factor tests, the three parameters exhibit decreasing influence in the following order: penetration depth, feed rate, and specimen rotational speed. By isolating the individual effect of each factor, these experiments delimit the allowable processing window and help avoid two undesirable regimes: excessively low values, which generate insufficient plastic deformation and thus a weak compressive residual stress; and excessively high values, which lead to over-stretching of the surface, intensified cyclic plasticity from repeated passes, and non-uniform rolling, all detrimental to the surface rolling strengthening of the gear shaft. Furthermore, the identified parameter ranges lay a sound foundation for the subsequent response surface methodology coupled with the CCD; the resulting interaction and prediction models for the residual stress under multi-parameter conditions substantially reduce the required number of experimental runs while improving model fitting accuracy.

3.3. Simulation-Based Analysis of Process Parameter Effects

Based on the single-factor experiments, three input factors, penetration depth (0.05–0.20 mm), feed rate (0.01–0.10 mm/r), and specimen rotational speed (120–840 rpm), are each investigated at five levels within their working ranges, and the corresponding coded levels are listed in Table 5. The rolled journal surface compressive residual stress and the strengthened layer depth served as the response variables.

Table 5. Process factors and their coded levels in the central composite design.

Corresponding Coded Level	A: Surface Penetration Depth (mm)	B: Specimen Rotational Speed (r/min)	C: Rolling Feed Rate (mm/r)
$-\alpha$	0.05	120	0.01
-1	0.07	360	0.03
0	0.10	600	0.05
1	0.15	720	0.07
$+\alpha$	0.20	840	0.10

The CCD consisted of 17 runs in total, comprising 14 factorial and axial runs together with three replicated center points. A separate finite-element model was constructed and solved for each factor-level combination. The rolling conditions applied in the 17 experimental runs, together with the resulting response values, are listed in Table 6.

Table 6. Experimental design matrix and corresponding response values.

No.	Factors			Response Parameters	
	Penetration Depth (mm)	Specimen Rotational Speed (r/min)	Feed Rate (mm/r)	Residual Stress (MPa)	Strengthened Layer Depth (mm)
1	0.10	600	0.01	−522.286	0.6832
2	0.15	720	0.07	−592.502	0.8596
3	0.10	600	0.05	−569.271	0.7203
4	0.10	600	0.10	−551.132	0.6703
5	0.10	600	0.05	−569.272	0.7192
6	0.15	720	0.03	−566.596	0.7943
7	0.10	840	0.05	−553.038	0.7142
8	0.07	300	0.07	−503.013	0.6344
9	0.15	300	0.07	−583.967	0.8169
10	0.07	300	0.03	−479.574	0.5942
11	0.07	720	0.03	−489.296	0.6379
12	0.10	600	0.05	−569.273	0.7192
13	0.15	300	0.03	−572.012	0.7404
14	0.10	120	0.05	−549.103	0.7142
15	0.05	600	0.05	−432.763	0.5594
16	0.07	720	0.07	−510.279	0.6688
17	0.20	600	0.05	−557.964	0.8391

Using the data compiled in Table 6, regression models were constructed to describe the dependence of the rolled journal surface residual compressive stress and the strengthened-layer depth on the three process parameters, namely the penetration depth, specimen rotational speed, and rolling feed rate. Linear, two-factor interaction (2FI), and quadratic forms were examined as candidate models, and a comparison of their fitting performance is presented in Table 7.

Table 7. Comparison of the fitting performance of the regression models.

Response	Coefficient of Determination	Linear	2FI	Quadratic
Residual stress	R^2	0.5914	0.5973	0.9752
	R^2_{adj}	0.4956	0.3540	0.9417
	R^2_{pred}	0.2664	0.1415	0.7361
Stress depth	R^2	0.8655	0.8345	0.9666
	R^2_{adj}	0.8345	0.8130	0.9236
	R^2_{pred}	0.7174	0.6237	0.6946

As indicated by the fitting results in Table 7, the quadratic model exhibits the best agreement with the experimental data and is hence employed in the subsequent regression analysis. The resulting empirical expressions correlate each response with the coded parameter values and take the following general form:

$$Y = \beta_0 + \sum_{i=1}^{3} \beta_i X_i + \sum_{i=1}^{3} \beta_{ii} X_i^2 + \sum_{i=1}^{3} \sum_{j=i+1}^{3} \beta_{ij} X_i X_j + \varepsilon \quad (28)$$

where Y is the response; β_0 represents the constant term; β_i denotes the coefficient of the linear term; β_{ii} indicates the coefficient of the quadratic term; β_{ij} is the coefficient of the interaction term; and ε is the random error. The model coefficients were determined by least-squares fitting, and stepwise regression is then applied to remove the insignificant terms, yielding the following simplified equations for the two responses:

$$\sigma = -592.86 - 49.11A - 6.61B - 13.54C - 2.49AB + 2.70AC - 4.36BC + 93.64A^2 + 15.28B^2 + 31.89C^2 \quad (29)$$

$$d = 0.8246 + 0.0929A + 0.0060B + 0.0069AB + 0.0350AC - 0.0151BC - 0.0440A^2 + 0.0029B^2 - 0.0410C^2 \quad (30)$$

The regression coefficients indicate that factor A (penetration depth) carries the largest absolute linear coefficient and hence exerts the strongest influence on both responses. The statistically significant interaction terms AB and AC indicate that penetration depth interacts strongly with both the rolling feed rate and the specimen rotational speed, as well as between the penetration depth and the rotational speed of the test specimen. In addition, the significant quadratic terms confirm that both responses depend nonlinearly on the rolling process parameters, which agrees well with the plastic-saturation behavior identified in the single-factor experiments. The adequacy of the regression models for the two responses, the rolled journal surface compressive residual stress and the strengthened layer depth, was assessed using three statistical indices, namely, R^2, adjusted R^2, and predicted R^2, with the corresponding values listed in Table 8. Normal-probability plots and residuals-versus-fitted diagrams (collectively referred to as residual assessments) are provided in the Figure 15. These performance indicators have the following explanations: values very close to one signal a tight match between modelled and observed outcomes, while a small difference between adjusted and projected results points to strong generalizability.

Table 8. Analysis of variance for the response surface regression equations.

Response	Adequate Precision	Coefficient of Variation (%)	F-Value	*p*-Value
Surface residual stress	10.53	1.96	29.72	<0.0001
Strengthened layer depth	15.62	3.23	22.51	0.0002

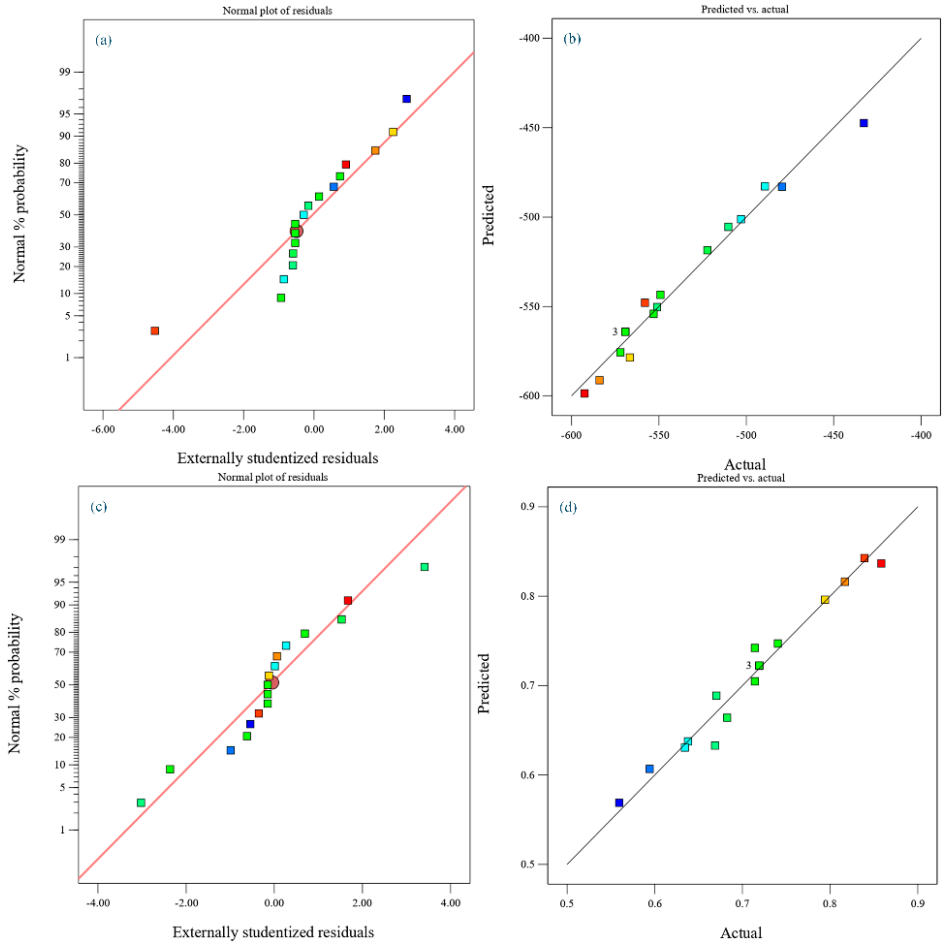


Figure 15. Diagnostic checks of model adequacy. (**a**) Residual analysis for the residual-stress model; (**b**) predicted versus actual values of the residual stress; (**c**) residual analysis for the strengthened-layer model; (**d**) predicted versus actual values of the strengthened-layer depth.

These two regression formulae were subsequently evaluated using analysis of variance (ANOVA), with the corresponding results compiled in Table 8. Both models are highly significant (F = 29.72 and 22.51, respectively; $p < 0.01$), and the individual parameter effects are statistically distinguishable. Moreover, the coefficients of variation (<5.0%) fall well below the 10% acceptability limit, indicating reproducible data, and the adequate precision ratios exceed 4. These results collectively confirm the reliability of the fitted models for further use.

To determine whether the parametric models produce consistent predictions under actual operating conditions, three extra parameter set configurations were randomly picked from the CCD domain, omitting the trials previously utilized for regression, and analyzed in complementary verification tests. Quantitative analysis is conducted on the gaps between the projected and observed data points, with these analytical results compiled and presented in Table 9.

Table 9. Results of the model-accuracy validation.

Verification Points	A (mm)	B (r/min)	C (mm/r)	Indicators	Forecast Value	Test Values	Relative Error (%)
1	0.15	600	0.05	Surface residual stress (MPa)	−597.649	−563.504	5.713
				Stress depth (mm)	0.638	0.599	6.012
2	0.10	360	0.05	Surface residual stress (MPa)	−560.623	−578.464	3.183
				Stress depth (mm)	0.712	0.695	2.216
3	0.10	600	0.03	Surface residual stress (MPa)	−545.403	−558.665	2.432
				Stress depth (mm)	0.682	0.664	2.731

Compared with the experimental data, the predicted surface compressive residual stress and strengthened layer depth exhibit maximum relative errors of only 5.71% and 6.01%, respectively, well within the 10% acceptance criterion. This confirms that the fitted models accurately reproduce the residual stress behavior of 30CrMoA gear-shaft journals across the investigated rolling parameter domain.

3.4. Multi-Objective Optimization of Process Parameters and Experimental Validation

Using the response surface models developed above, multi-objective optimization is performed to enhance the surface quality of gear shafts through rolling, following the approach in Ref. [45], to identify the optimal parameter combination, whose reliability is subsequently verified through confirmation experiments. The desirability function method is employed to determine the optimal process parameters by simultaneously maximizing the magnitude of the rolled surface residual compressive stress and the depth of the compressive-stress layer. By leveraging the in-built optimization tool integrated within the Design-Expert software (DEFORM V13.1), a comprehensive desirability index is calculated for each potential solution, and the ten combinations that ranked highest on this index are kept for further consideration. Since depending on just one outcome is not a reasonable choice, factors like parameter practicality and operational equipment capacity are also considered during the final selection, the selected best result is documented in Table 10.

Table 10. Candidate solutions ranked by overall desirability in the multi-objective optimization.

No.	A (mm)	B (r/min)	C (mm/r)	Surface Residual Stress (MPa)	Strengthened Layer Depth (mm)	D-Value
1	0.156	590.858	0.067	−601.592	0.823	0.8838
2	0.156	591.139	0.067	−601.592	0.823	0.88384
3	0.156	590.531	0.067	−601.591	0.822	0.88383
4	0.156	590.913	0.067	−601.593	0.823	0.88382

Table 10. *Cont.*

No.	A (mm)	B (r/min)	C (mm/r)	Surface Residual Stress (MPa)	Strengthened Layer Depth (mm)	D-Value
5	0.156	591.568	0.067	−601.593	0.823	0.88382
6	0.156	590.012	0.067	−601.591	0.821	0.88382
7	0.156	590.858	0.067	−601.589	0.823	0.88382
8	0.156	590.521	0.067	−601.589	0.823	0.88381
9	0.155	589.338	0.066	−601.653	0.821	0.88113
10	0.157	606.279	0.068	−601.317	0.824	0.86506

Combining the overall desirability factor (D) and the practical feasibility of the operational steps, the first set is picked out as the most suitable set of operating parameters: the rolling depth is 0.147 mm, the feeding speed is 0.066 mm per revolution, and the rotation speed of the processed part is 590 revolutions per minute. With this parameter set applied, the simulation model predicts a rolled journal surface residual compressive stress of −601.59 MPa together with a compressive-stress layer depth of 0.822 mm. An overall desirability of 0.884 is achieved, with every individual objective satisfying its specified constraints.

Following that, validation trials were performed using the parameters identified through the optimization process, to assess how consistent the multi-target optimization technique works when applied to real-world scenarios; the values obtained from actual testing were directly contrasted with the projections generated by the relevant model, as detailed in the corresponding Figures 16 and 17. Across all experimental parameter combinations, the numerical predictions agreed well with the experimental measurements. A separate analysis of the three single-factor test series yielded mean relative errors in surface residual stress of 6.42% for indentation depth, 7.67% for specimen rotational speed, and 6.06% for strengthening feed rate. The corresponding errors in the depth of the strengthened layer were 4.33%, 7.57%, and 4.94%, respectively. With all prediction errors below 8.0%, the simulation model demonstrated satisfactory accuracy in predicting both response variables. Moreover, the predicted trends closely followed the experimental data over the entire range of process parameters investigated. Figure 18 presents the results used to evaluate the improvement in rolled journal surface quality achieved through optimization of the strengthening process and to examine the microstructural evolution of the surface layer under the optimal rolling conditions.

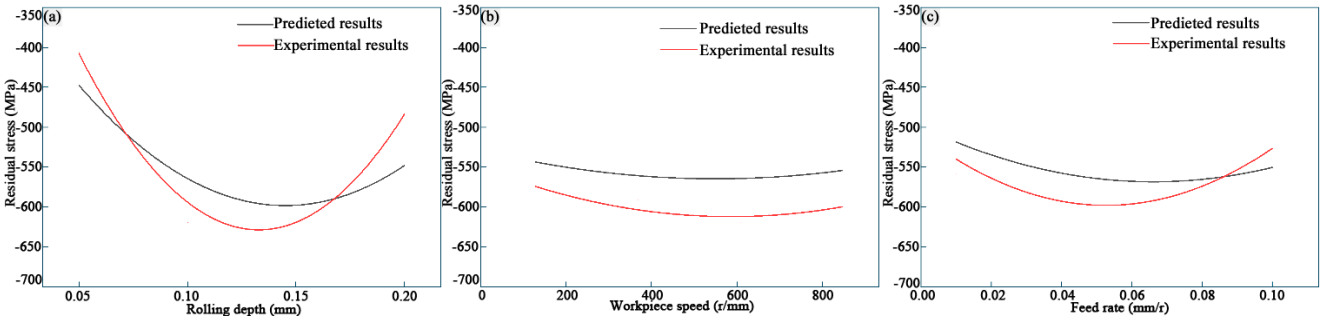


Figure 16. Comparison between model-predicted and measured values of rolled journal surface residual stress. (**a**) Surface strengthening rolling depth; (**b**) specimen rotational speed; (**c**) feed rate.

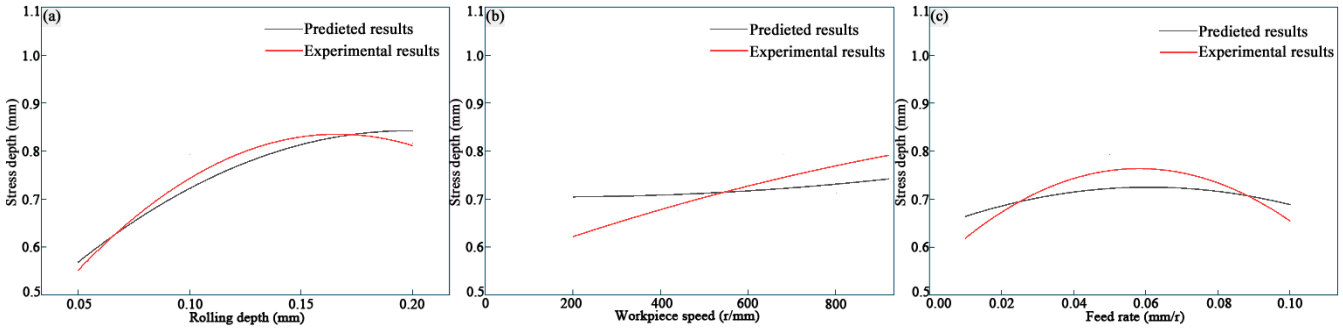


Figure 17. Model predictions of compressive-stress layer depth against experimental data. (**a**) Surface strengthening rolling depth; (**b**) specimen rotational speed; (**c**) feed rate.

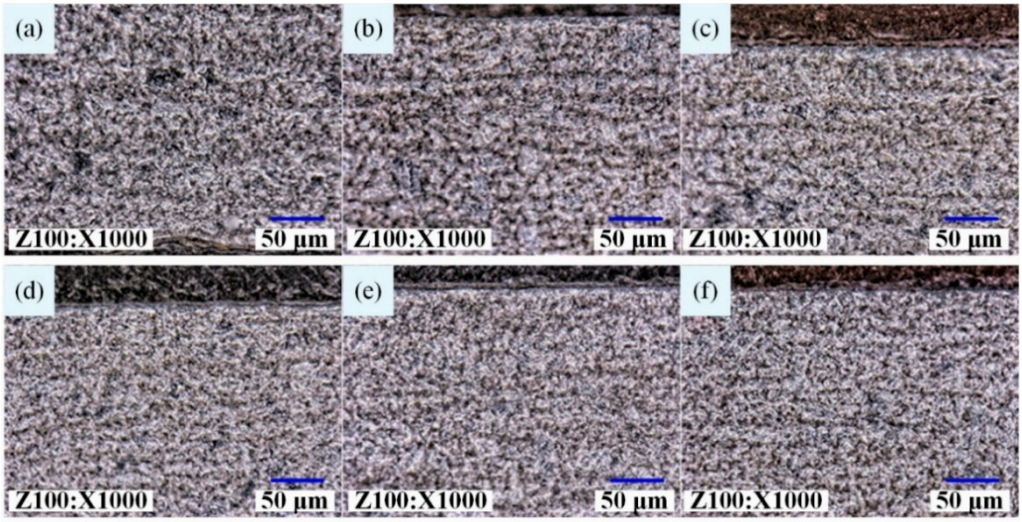


Figure 18. Cross-sectional microstructures corresponding to different processing conditions: (**a**) initial condition; (**b**–**e**) strengthening rolling depths of 0.05, 0.10, 0.15, and 0.20 mm, respectively; and (**f**) optimal deep-rolling parameters (depth = 0.147 mm, rotational speed = 590 r/min, and feed = 0.06 mm/r).

This explanation is built on mutually consistent indirect proof, such as the tested microhardness change along a gradient, the distribution of remaining internal forces, and the characteristics of plastic movement spotted through experiments. Given the well-established correlation among process parameters, plastic flow, work hardening, and microstructure evolution under severe plastic deformation conditions [48], this interpretation rests on a sound methodological basis. As the penetration depth increases, the near-surface grains are subjected to increasingly severe plastic deformation. At a depth of 0.05 mm, the grains exhibit only slight elongation along the rolling direction; the deformed layer remains thin, and the grain boundaries are still clearly distinguishable. Increasing the depth to 0.10 mm progressively flattens the equiaxed grains into a fibrous morphology and substantially thickens the deformed layer. Upon reaching 0.15 mm, strong flattening and elongation of the surface grains occur: the flow-line pattern becomes considerably denser, and fragmentation of the initial grain boundaries leads to the formation of numerous subgrains and dislocation cells. At 0.20 mm, the deformed layer thickens further, and the grain structure becomes still finer, however, these changes are accompanied by pronounced pile-up of surface material and micro-wrinkling, together with a slight loss of uniformity in the deformed zone. As shown in Figure 18f, the microstructure produced under the optimized parameter combination (0.147 mm, 590 r/min, 0.06 mm/r) exhibits finer grains, more uniform plastic deformation, and a thicker deformed layer than any single-factor case, reflecting a superior surface strengthening effect. This confirms that the coupling of a relatively large penetration

depth with moderate rotational speed and feed rate produces large yet uniform plastic deformation in the surface layer, leading to the most favourable grain refinement.

4. Conclusions

(1) A gradient-type compressive residual stress field is established in the near-surface layer of the gear-shaft journal through rolling strengthening. Beneath the surface, compressive stress of 400–600 MPa prevails, attaining its maximum value of over 800 MPa at a depth of roughly 0.20 mm, in the deeper substrate, mechanical balance gives rise to a weak tensile counterpart in the range of 100–180 MPa. Benefiting from this favourable stress state, both fatigue crack nucleation and growth can be effectively suppressed.

(2) Single-factor experiments show the penetration depth to be the dominant parameter governing the residual stress field, followed by the feed rate and the specimen rotational speed. Increasing the penetration depth markedly raises the compressive stress and the strengthened layer depth, but beyond 0.10 mm, plastic saturation and the intensified cyclic plasticity from repeated passes cause a slight drop in surface stress. The optimal ranges are 600–720 r/min for rotational speed and 0.05–0.07 mm/r for feed rate; outside these ranges, an excessive plastic strain gradient or non-uniform rolling coverage degrades the strengthening effect.

(3) Quadratic regression models for the rolled journal surface compressive residual stress and the strengthened layer depth were developed using response surface methodology with a central composite design. ANOVA confirms that both models are highly significant ($p < 0.01$), with signal-to-noise ratios above 4 and coefficients of variation below 5.0%. Confirmation tests yield maximum relative errors of only 5.71% and 6.01%, well within 10%, verifying the models' reliability in predicting residual stress behavior under various rolling conditions.

(4) Multi-objective optimization identifies an optimal parameter set, 0.147 mm penetration depth, 590 r/min specimen rotational speed, and 0.067 mm/r feed rate, under which the model predicts a surface compressive residual stress of −601.59 MPa and a strengthened layer depth of 0.822 mm. The corresponding microstructure exhibits uniformly refined grains and a dense deformed layer, achieving a favourable balance between high surface stress and deep strengthening, thereby corroborating the reliability and effectiveness of the optimization.

Author Contributions: Conceptualization, Y.W. and X.W.; methodology, X.W. and J.R.; software, J.R. and Y.W.; validation, X.W., Y.W. and J.R.; formal analysis, J.R., Y.W. and X.W.; investigation, X.W. and Y.W.; resources, X.W. and Y.W.; data curation, Y.W. and J.R.; writing—original draft preparation, X.W. and Y.W.; writing—review and editing, X.W., Y.W. and J.R.; visualization, X.W. and Y.W.; supervision, X.W. and J.R.; project administration, Y.W. and J.R. All authors have read and agreed to the published version of the manuscript.

Funding: This research was funded by the National Natural Science Foundation Sponsored Project (Project Approval Number: 52475257), the National Key Research and Development Program Project (Grant No. 2023YFB3406301), the Fund Project for Technological Field of National Defense Science and Technology Plan 173 (2024-JCJQ-JJ-2020) and (2024-JCJQ-JJ-2043), the Marine Propulsion Research and Development (MPRD) Program (Grant No. MG20220203).

Institutional Review Board Statement: Not applicable.

Informed Consent Statement: Not applicable.

Data Availability Statement: All relevant data are provided within the manuscript.

Acknowledgments: The authors would like to thank the Huaqiao University (HQU) and Heilongjiang Institute of Technology (HLJIT) for their support. Authors sincerely appreciate all participants for their contributions.

Conflicts of Interest: The authors declare no conflicts of interest.

References

1. Singh, T.; Sengar, S. Least life analysis of diesel locomotive crankshaft. *Mater. Today Proc.* **2021**, *44*, 4369–4374. [CrossRef]
2. Aliakbari, K.; Nejad, R.; Mamaghani, T.; Pouryamout, P.; Asiabaraki, H. Failure analysis of ductile iron crankshaft in compact pickup truck diesel engine. *Structures* **2022**, *36*, 482–492. [CrossRef]
3. Luo, Y.; Yue, G.; Chen, B.; Huang, B.; Liu, F.; Zhou, L.; Mao, X.; Deng, S.; Du, J.; Liu, K. Fatigue fracture analysis of the 42CrMo4 crankshaft used for mining dump truck. *Eng. Fail. Anal.* **2023**, *154*, 107724. [CrossRef]
4. Fu, J.; Sun, S.; Gong, X.; Shen, S.; Jiang, N.; Juan, J. Research on the Accelerated Fatigue Experiment Method of the Crankshaft Based on a Modified Particle Filtering Algorithm and the Fatigue Crack Growth Property. *Materials* **2026**, *19*, 481. [CrossRef] [PubMed]
5. Aliakbari, K. Failure analysis of four-cylinder diesel engine crankshaft. *J. Braz. Soc. Mech. Sci. Eng.* **2019**, *41*, 30. [CrossRef]
6. Aliakbari, K.; Nejad, R.; Toroq, S.; Macek, W.; Branco, R. Assessment of unusual failure in crankshaft of heavy-duty truck engine. *Eng. Fail. Anal.* **2022**, *134*, 106085. [CrossRef]
7. Wang, F.; Xia, J.Q.; Xu, X.; Cai, Y.F.; Ni, S.Y.; Que, H.B. Torsional vibration-considered energy management strategy for power-split hybrid electric vehicles. *J. Clean. Prod.* **2021**, *296*, 126399. [CrossRef]
8. Španiel, M.; Horváth, J.; Bartošák, M. Multiaxial low-cycle thermo-mechanical fatigue of a low-alloy martensitic steel: Cyclic mechanical behaviour, damage mechanisms and life prediction. *Int. J. Fatigue* **2021**, *151*, 106383. [CrossRef]
9. Zhou, C.; Wang, H.; Hou, S.; Han, Y. A hybrid physics-based and data-driven method for gear contact fatigue life prediction. *Int. J. Fatigue* **2023**, *175*, 107763. [CrossRef]
10. Li, X.; Liang, G.; Ling, X.; Xu, C.; Xu, J. An investigation of relationships between statistical dispersion of crankshaft's fatigue properties and initial damage. *Eng. Fail. Anal.* **2023**, *154*, 107680. [CrossRef]
11. Noronha, D.J.; Sharma, S.; Prabhu Parkala, R.; Shankar, G.; Kumar, N.; Doddapaneni, S. Deep Rolling Techniques: A Comprehensive Review of Process Parameters and Impacts on the Material Properties of Commercial Steels. *Metals* **2024**, *14*, 667. [CrossRef]
12. Nguyen, T.T.; Nguyen, T.A.; Trinh, Q.H.; Ba Le, X.; Hai Pham, L.; Hung Le, L. Artificial neural network-based optimization of operating parameters for minimum quantity lubrication-assisted burnishing process in terms of surface characteristics. *Neural Comput. Appl.* **2022**, *34*, 7005–7031. [CrossRef]
13. Kluz, R.; Antosz, K.; Trzepieciński, T.; Bucior, M. Modelling the influence of slide burnishing parameters on the surface roughness of shafts made of 42CrMo4 heat-treatable steel. *Materials* **2021**, *14*, 1175. [CrossRef] [PubMed]
14. Heikebrügge, S.; Breidenstein, B.; Bergmann, B.; Dänekas, C.; Schaumann, P.; Schubnell, J. Identification of material properties for finite element simulation of the deep rolling process applied to welded joints. *Procedia CIRP* **2022**, *115*, 30–35. [CrossRef]
15. Pertoll, T.; Buzzi, C.; Leitner, M.; Boronkai, L. Numerical parameter sensitivity analysis of residual stresses induced by deep rolling for a 34CrNiMo6 steel railway axle. *Int. J. Adv. Manuf. Technol.* **2024**, *131*, 483–504. [CrossRef]
16. Morrev, P.G.; Gordon, V.A. Simulation of surface hardening in the deep rolling process by means of an axial symmetric nodal averaged finite element. *J. Phys. Conf. Ser.* **2018**, *973*, 012013. [CrossRef]
17. Fonseca, L.G.A.; Faria, A.R.D. Crankshaft deep rolling analysis through energy balance simulation output. *J. Braz. Soc. Mech. Sci. Eng.* **2019**, *41*, 430. [CrossRef]
18. Bialowas, J.; Pletz, M.; Gapp, S.; Maierhofer, J. A method to reduce computation time in finite element simulations of deep rolling. *Procedia Struct. Integr.* **2023**, *46*, 49–55. [CrossRef]
19. Kinner-Becker, T.; Sölter, J.; Karpuschewski, B. A simulation-based analysis of internal material loads and material modifications in multi-step deep rolling. *Procedia CIRP* **2020**, *87*, 515–520. [CrossRef]
20. Kinner-Becker, T.; Hettig, M.; Sölter, J.; Meyer, D. Analysis of internal material loads and Process Signature Components in deep rolling. *CIRP J. Manuf. Sci. Technol.* **2021**, *35*, 400–409. [CrossRef]
21. Kinner-Becker, T.; Sölter, J. Influence of initial stress on the residual stress generated by deep rolling. *Procedia CIRP* **2023**, *117*, 128–132. [CrossRef]
22. Fonseca, L.G.A.; Faria, A.R.D. A deep rolling finite element analysis procedure for automotive crankshafts. *J. Strain Anal. Eng. Des.* **2018**, *53*, 178–188. [CrossRef]
23. Kumar, A.; Rath, S.; Kumar, M. Simulation of plate rolling process using finite element method. *Mater. Today Proc.* **2021**, *42*, 650–659. [CrossRef]

24. Schubnell, J.; Dahmen, M.; Luke, M. Strength improvement of laser beam welded joints in cold worked high-manganese-steel by means of deep rolling. *Procedia CIRP* **2022**, *111*, 457–461. [CrossRef]
25. Dänekas, C.; Heikebrügge, S.; Schubnell, J.; Schaumann, P.; Breidenstein, B.; Bergmann, B. Influence of deep rolling on surface layer condition and fatigue life of steel welded joints. *Int. J. Fatigue* **2022**, *162*, 106994. [CrossRef]
26. Heikebrügge, S.; Breidenstein, B.; Bergmann, B.; Dänekas, C.; Schaumann, P. Experimental and Numerical Investigations of the Deep Rolling Process to Analyze the Local Deformation Behavior of Welded Joints. *J. Manuf. Mater. Process.* **2022**, *6*, 50. [CrossRef]
27. Reggiani, B.; Olmi, G. Experimental investigation on the effect of shot peening and deep rolling on the fatigue response of high strength fasteners. *Metals* **2019**, *9*, 1093. [CrossRef]
28. Martins, A.M.; Oliveira, D.A.D.; de Castro Magalhães, F.; Abrão, A.M. Relationship between surface characteristics and the fatigue life of deep rolled AISI 4140 steel. *Int. J. Adv. Manuf. Technol.* **2023**, *129*, 1127–1143. [CrossRef]
29. Dos, S.F.F.; Silva, S.D.C.; Abrão, A.M.; Denkena, B.; Breidenstein, B.; Meyer, K. Influence of the carbon content on the surface integrity of deep rolled steels. *J. Tribol.* **2021**, *143*, 081702. [CrossRef]
30. Chen, Z.W.; Wang, F.; Zhang, H.B.; Chen, Z.G.; He, Q.L. Performance and safety evaluation of rack vehicle in mountainous regions under pulsating wind loads. *Mech. Based Des. Struct. Mach.* **2025**, *54*, 2553887. [CrossRef]
31. Caddemi, S. Computational aspects of the integration of the von Mises linear hardening constitutive laws. *Int. J. Plast.* **1994**, *10*, 935–956. [CrossRef]
32. Łach, Ł. Recent Advances in Laser Surface Hardening: Techniques, Modeling Approaches, and Industrial Applications. *Crystals* **2024**, *14*, 726. [CrossRef]
33. Xu, Z.; Wang, S.; Gao, L.; Qiao, X.; Cui, Y. Fatigue life analysis model of crankshaft under uncertain working conditions based on physical-data collaboration. *J. Eng. Res.* **2025**, *13*, 1241–1249. [CrossRef]
34. Ma, K.; Du, J.; Liu, Y.; Chen, X. Torsional vibration attenuation of a closed-loop engine crankshaft system via the tuned mass damper and nonlinear energy sink under multiple operating conditions. *Mech. Syst. Signal Process.* **2024**, *207*, 110941. [CrossRef]
35. Wang, Y.P.; Luo, Y.C.; Mo, Q.Y.; Huang, B.; Wang, S.Y.; Mao, X.F.; Zhou, L. Failure analysis and improvement of a 42CrMo crankshaft for a heavy-duty truck. *Eng. Fail. Anal.* **2023**, *153*, 107567. [CrossRef]
36. Jalili, A.; Ashtiani, H.R. Numerical analysis and neural-network modeling for predicting the thermo-viscoplastic behavior of Cu/AA2030 panel during the hot rolling process. *Multiscale Multidiscip. Model. Exp. Des.* **2026**, *9*, 179. [CrossRef]
37. Rashad, M.; Magdi, A.; Ahmed, M.E.; Metwalli, S.M. Optimal design of round-oval-round roll pass for the steel bar rolling process. *J. Eng. Appl. Sci.* **2024**, *71*, 224. [CrossRef]
38. Song, J.; Lan, J.; Zhu, L.; Jiang, Z.; Zhang, Z.; Han, J.; Ma, C. Finite Element Simulation and Microstructural Analysis of Roll Forming for DP590 High-Strength Dual-Phase Steel Wheel Rims. *Materials* **2024**, *17*, 3795. [CrossRef] [PubMed]
39. Wang, A.; Xue, H.; Bayraktar, E.; Yang, Y.; Saud, S.; Chen, P. Analysis and Control of Twist Defects of Aluminum Profiles with Large Z-Section in Roll Bending Process. *Metals* **2020**, *10*, 31. [CrossRef]
40. Wang, Y.; Zeng, X.; Chen, H.; Yang, X.; Wang, F.; Zeng, L. Modified Johnson-Cook constitutive model of metallic materials under a wide range of temperatures and strain rates. *Results Phys.* **2021**, *27*, 104498. [CrossRef]
41. Zhang, S.; Shu, X.; Wang, J.; Xia, Y. Constitutive Model of 30CrMoA Steel with Strain Correction. *Metals* **2020**, *10*, 1214. [CrossRef]
42. Wuertemberger, L.; Palazotto, A.N. Evaluation of Flow and Failure Properties of Treated 4130 Steel. *J. Dyn. Behav. Mater.* **2016**, *2*, 207–222. [CrossRef]
43. Zhong, B.; Qiang, X.; Yu, Z.; Hu, S.; Yang, H. Analysis and prediction of maximum contact stress and depth by ultrasonic surface rolling with elastic–plastic theory. *Int. J. Adv. Manuf. Technol.* **2022**, *124*, 3225–3239. [CrossRef]
44. Zhou, Y.; Chu, X.; Zang, S.; Sun, J.; Yang, L.; Gao, J. Effect of surface integrity on fatigue life of 7075-T6 aluminum alloy by combination of fine turning with hydrostatic deep rolling. *Arch. Civ. Mech. Eng.* **2023**, *23*, 41. [CrossRef]
45. Hong, Y.; Wang, L.Z.; Zhang, J.F.; Gao, Z.W. 3D Elastoplastic Model for Fine-Grained Gassy Soil Considering the Gas-Dependent Yield Surface Shape and Stress-Dilatancy. *J. Eng. Mech.* **2020**, *146*, 04020037. [CrossRef]
46. Zhao, Y.B.; Zhao, J.H. The effects of tab cooling on thermal behavior and thermal runaway suppression in lithium-ion cell module. *J. Power Sources* **2026**, *661*, 238657. [CrossRef]
47. He, R.; Dai, Y.H.; Jin, J.J.; Yan, J.; Liu, D. The effects of time preferences on farmers' energy-saving and emission-reducing behavior of agricultural machinery in a gain-loss dual context: Evidence from rural China. *Energy* **2025**, *341*, 139325. [CrossRef]
48. Ni, Z.L.; Han, B.L.; Nazarov, A.A.; Yuan, Z.P.; Li, N.N.; Li, H.; Sun, C.Y.; Yang, J.W. Enhanced formation quality and mechanical properties of ultrasonic spot welding of TA2 Ti sheets by pure Al coating. *J. Manuf. Processes* **2025**, *156*, 1–16. [CrossRef]

Disclaimer/Publisher's Note: The statements, opinions and data contained in all publications are solely those of the individual author(s) and contributor(s) and not of MDPI and/or the editor(s). MDPI and/or the editor(s) disclaim responsibility for any injury to people or property resulting from any ideas, methods, instructions or products referred to in the content.